Rapid Communications

Characteristics of shearing motions in incompressible isotropic turbulence

T. Watanabe,* K. Tanaka, and K. Nagata
Department of Aerospace Engineering, Nagoya University, Nagoya 464-8603, Japan

(Received 12 November 2019; accepted 17 June 2020; published 7 July 2020)

Regions with shearing motions are investigated in isotropic turbulence with the triple decomposition, by which a velocity gradient tensor is decomposed into three components representing an irrotational straining motion, a rotating motion, and a shearing motion. A mean flow around the shearing motions shows that a thin shear layer is sustained by a biaxial strain, which is consistent with Burgers' vortex layer. The thickness of each shear layer is well predicted by Burgers' vortex layer. A comparison between genuine turbulence and a random velocity field confirms that the biaxial strain acting on the shear is a dynamical consequence from the Navier-Stokes equations rather than from a kinematic relation. The interplay between the shear and biaxial strain causes enstrophy production and strain self-amplification. For a wide range of Reynolds number, the shear is strong enough for the instability to cause a roll-up of the shear layer, where the perturbation grows much faster than large-scale turbulent motions.

DOI: 10.1103/PhysRevFluids.5.072601

Turbulence is present in the motion of fluids, and governs many mechanisms existing in physics problems [1]. Small-scale intermittency is one of the most important natures of turbulence [2], and is associated with statistical and structural properties of turbulence. In a statistical sense, one can observe the intermittent behavior of turbulence in the scaling exponents for structure functions or probability density functions of small-scale quantities such as enstrophy [3,4]. On the other hand, spatiotemporal distributions of these small-scale quantities often display turbulent structures underlying their intermittent features [2,5]. The importance of structures in turbulence is extensively discussed in existing literature (e.g., [6]). Although both statistical and structural approaches are necessary in understanding turbulence, investigating turbulent structures possibly helps us understand the physics of turbulence associated with the intermittency.

One of the most well-known small-scale turbulent structures is a tubular vortex with intense vorticity [2]. The vortices somehow resemble Burgers' vortex tube, which is one of a few exact, steady solutions of Navier-Stokes equations [7]. They were found in most turbulent flows [5,8–10], leading to discussion on the dynamical processes responsible for the formation of the vortex tubes. In this context, a sheetlike structure with moderate vorticity received attention in previous studies, which suggested that the vortex tubes are generated by a roll-up of the sheets by the Kelvin-Helmholtz instability [11,12]. A vortex sheet is essentially a layer of intense shear, which contributes to moderately large vorticity and strain [1]. Therefore, the vortex sheet is called a shear layer in the present Rapid Communication. Regions with shearing motions are expected to be important in dynamical aspects of turbulence [6]. Thin shear layers can be related to an active interscale energy transfer toward scales smaller than the Kolmogorov scale, and these structures can be potential quasisingularities of Navier-Stokes equations [13]. There is a layer analog of Burgers' vortex tube, which is called Burgers' vortex layer [7], whose relation to the shear layers in turbulence is, however, not clear so far.

*watanabe.tomoaki@c.nagoya-u.jp

TABLE I. Computational and physical parameters of DNS and random velocity.

Run	NS1	NS2	NS3	NS4	NS5	R1
N	256	512	1024	2048	4096	1024
L/L_0	5.8	5.3	4.5	4.5	5.0	19.3
Δ/η	0.83	0.82	0.84	0.82	0.81	1.1
$\mathrm{Re}_L = u'L_0/\nu$	122	361	1092	2709	5800	194
$\mathrm{Re}_\lambda = u'\lambda/\nu$	43	72	128	202	296	60

Studying turbulent structures requires an identification scheme of the structures which provides their location, spatial extent, and orientation. Unlike the vortex tubes, the identification of the shear layers is more complicated [14]. Even though shearing motions are possibly important in many phenomena in turbulence, they have hardly been studied except with visualization of small-scale layer structures, which might be related to shear layers in turbulence. This is because there have been no reliable tools to quantify shearing motions in turbulence. A triple decomposition of a velocity gradient tensor is particularly useful for studying shearing motions because it yields a tensor representing shear [15,16]. The triple decomposition of the three-dimensional velocity gradient tensor has become recently available in [17]. In this study, a new method based on the triple decomposition is proposed for identifying the shear direction in three-dimensional velocity fields, enabling us to systematically study the flow field associated with shearing motions.

Direct numerical simulations (DNSs) of forced, homogeneous isotropic turbulence are carried out to study shearing motions (NS1–5 in Table I). The DNS uses a linear forcing [18] for achieving a statistically stationary state. The DNS code is the same as [19], and solves incompressible Navier-Stokes equations with the fourth-order central difference scheme and third-order Runge-Kutta scheme. The DNS is performed with a periodic box with size L^3, which is represented by N^3 grid points. The DNS is initialized with artificial velocity fluctuations generated by a diffusion process [20]. Time is advanced for more than ten times the integral timescale, by which influences of the initial condition disappear. Statistics are computed with a spatial average in the computational domain and an ensemble average of different time instances, where the average is denoted by $\langle\ \rangle$. Table I shows the grid size $\Delta = L/N$ divided by the Kolmogorov scale $\eta = (\nu^3/\varepsilon)^{1/4}$ and L divided by the integral scale $L_0 = u'^3/\varepsilon$, where ε is the turbulent kinetic energy dissipation rate, ν is the kinematic viscosity, and u' is the root-mean-squared (rms) velocity fluctuation. The table also shows the Reynolds number Re_L and the turbulent Reynolds number Re_λ defined with the Taylor microscale $\lambda = \sqrt{15\nu u'^2/\varepsilon}$.

A divergence-free, random velocity field with a prescribed energy spectrum is also analyzed for understanding the kinematic natures of shearing motions. This velocity field is generated by applying the inverse Fourier transform to velocity vectors in wave-number space with a random phase. The random velocity data R1 in Table I is the same as the one used in [21], and further details of the parameters and spectral shape can be found there.

The shearing motion is studied with the triple decomposition [15], by which $\nabla \boldsymbol{u}$ is decomposed as $\nabla \boldsymbol{u} = \nabla \boldsymbol{u}_R + \nabla \boldsymbol{u}_E + \nabla \boldsymbol{u}_S$, where $\nabla \boldsymbol{u}_R$, $\nabla \boldsymbol{u}_E$, and $\nabla \boldsymbol{u}_S$ are associated, respectively, with rotation, elongation (deformation without shear), and shear. Hereafter, a component of a second-order tensor is denoted with subscripts, e.g., $(\nabla \boldsymbol{u})_{ij} = \partial u_i/\partial x_j$. The triple decomposition calculates $\nabla \boldsymbol{u}_S$ as

$$(\nabla \boldsymbol{u}_S)_{ij} = (\nabla \boldsymbol{u})_{ij} - \mathrm{sgn}[(\nabla \boldsymbol{u})_{ij}] \min[|(\nabla \boldsymbol{u})_{ij}|, |(\nabla \boldsymbol{u})_{ji}|], \tag{1}$$

for $(i, j) = (1, 2)$ and $(1, 3)$ while other components are zero. $\nabla \boldsymbol{u}_E$ and $\nabla \boldsymbol{u}_R$ are symmetric and antisymmetric parts of $(\nabla \boldsymbol{u}) - (\nabla \boldsymbol{u}_S)$, respectively. Equation (1) ensures that $\nabla \boldsymbol{u}_S$ represents simple shear although the intensity of extracted shearing motions depends on coordinates where the decomposition is applied. Therefore, Eq. (1) should be applied in a basic reference frame, which is chosen from reference frames obtained with three sequential rotational transformations $Q(\theta_1, \theta_2, \theta_3)$

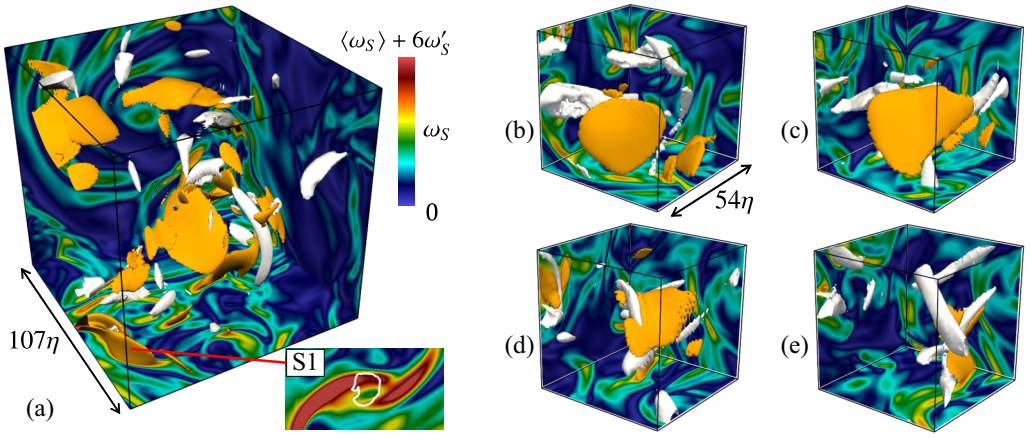

FIG. 1. (a) Isosurfaces of $\omega_R = \langle\omega_R\rangle + 4\omega'_R$ (white) and $\omega_S = \langle\omega_S\rangle + 4\omega'_S$ (orange). Color contour of ω_S and isoline of $\omega_R = \langle\omega_R\rangle + 4\omega'_R$ in S1 are also shown here. (b)–(e) Evolution of isosurfaces of $\omega_R = \langle\omega_R\rangle + 4\omega'_R$ (white) and $\omega_S = \langle\omega_S\rangle + 4\omega'_S$ (orange), where time is advanced from (b) to (e) with a time interval of $1.7\tau_\eta$. All results are taken from NS3.

with angles θ_i. The basic reference frame is defined such that the norm of $(\nabla \boldsymbol{u}_S)_{ij}$ assumes the maximum value among all reference frames [15]. The decomposition applied in the basic reference frame can effectively extract the shear contribution to the velocity gradient tensor with Eq. (1). The basic reference frame is determined with the numerical procedure presented in [17]. Once the decomposition is applied in the basic reference frame, the decomposed tensors in the original coordinate are obtained with the inverse of Q.

The shear intensity is represented by $\omega_S = \sqrt{(\boldsymbol{\omega}_S)_i(\boldsymbol{\omega}_S)_i}$, where $(\boldsymbol{\omega}_S)_i = \varepsilon_{ijk}(\nabla \boldsymbol{u}_S)_{jk}$ is an i-directional component of a vorticity vector of the shear tensor (ε_{ijk}: Levi-Civita symbol). Similarly, the intensities of rotation and elongation are given by $\omega_R = \sqrt{(\boldsymbol{\omega}_R)_i(\boldsymbol{\omega}_R)_i}$ and $s_E = \sqrt{2(\nabla \boldsymbol{u}_E)_{ij}(\nabla \boldsymbol{u}_E)_{ij}}$, respectively, with $(\boldsymbol{\omega}_R)_i = \varepsilon_{ijk}(\nabla \boldsymbol{u}_R)_{jk}$. Figure 1(a) shows isosurfaces of $\omega_S = \langle\omega_S\rangle + 4\omega'_S$ and $\omega_R = \langle\omega_R\rangle + 4\omega'_R$ (f': a rms fluctuation of f) in NS3. Shear layers are visualized by thin sheetlike structures of ω_S while vortex tubes are identified for ω_R. A vortex tube exists between two intense shear regions in S1. A two-dimensional profile of ω_S and isoline of ω_R are also shown for S1. The visualized flow pattern is similar to a contour plot of vorticity in the Kelvin-Helmholtz instability [22], indicating that a vortex with large ω_R is generated in the shear layer. One of the shear layers is tracked over 5.1 times the Kolmogorov timescale $\tau_\eta = \sqrt{\nu/\varepsilon}$ in Figs. 1(b)–1(e). The shear layer evolves with time, and eventually disappears to form a tubular vortex with strong rotation. The timescale of this vortex formation is of the order of the Kolmogorov timescale. These shear layers are short-lived, but certainly exist for a finite time period.

No matter how strong shearing motions are in flow structures defined with ω_S, we can find local maxima of ω_S in the structures. Therefore, a mean flow field associated with shearing motions is investigated with averages taken around local maxima of ω_S, which can be uniquely identified with the Hessian matrix $\partial^2\omega_S/\partial x_i \partial x_j$ without any thresholds. Each point of the local maxima of ω_S is investigated in relation to the shear direction represented in a local shear coordinate $(\zeta_1, \zeta_2, \zeta_3)$, whose directions are given by unit vectors $\boldsymbol{n}_1$, $\boldsymbol{n}_2$, and $\boldsymbol{n}_3$, respectively. Here, we assume an orthogonal, right-hand coordinate system. The Cartesian coordinate used in the DNS is $\boldsymbol{x} = (x, y, z)$, where $\boldsymbol{n}_i$ is expressed as $[(\boldsymbol{n}_i)_x, (\boldsymbol{n}_i)_y, (\boldsymbol{n}_i)_z]$. The shear coordinate is defined so that the shear is expressed solely with the derivative of $\boldsymbol{n}_3$-directional velocity with respect to ζ_2, where $\boldsymbol{n}_1$ can be determined as the vorticity direction of the shear tensor, $\boldsymbol{n}_1 = \boldsymbol{\omega}_S/|\boldsymbol{\omega}_S|$. The norm of the shear tensor does not change with the orthogonal coordinate transformation. Therefore, $(\nabla \boldsymbol{u}_S)_{3,2}$ has the largest value in the shear coordinate among all possible coordinate systems with $\boldsymbol{n}_1 = \boldsymbol{\omega}_S/|\boldsymbol{\omega}_S|$.

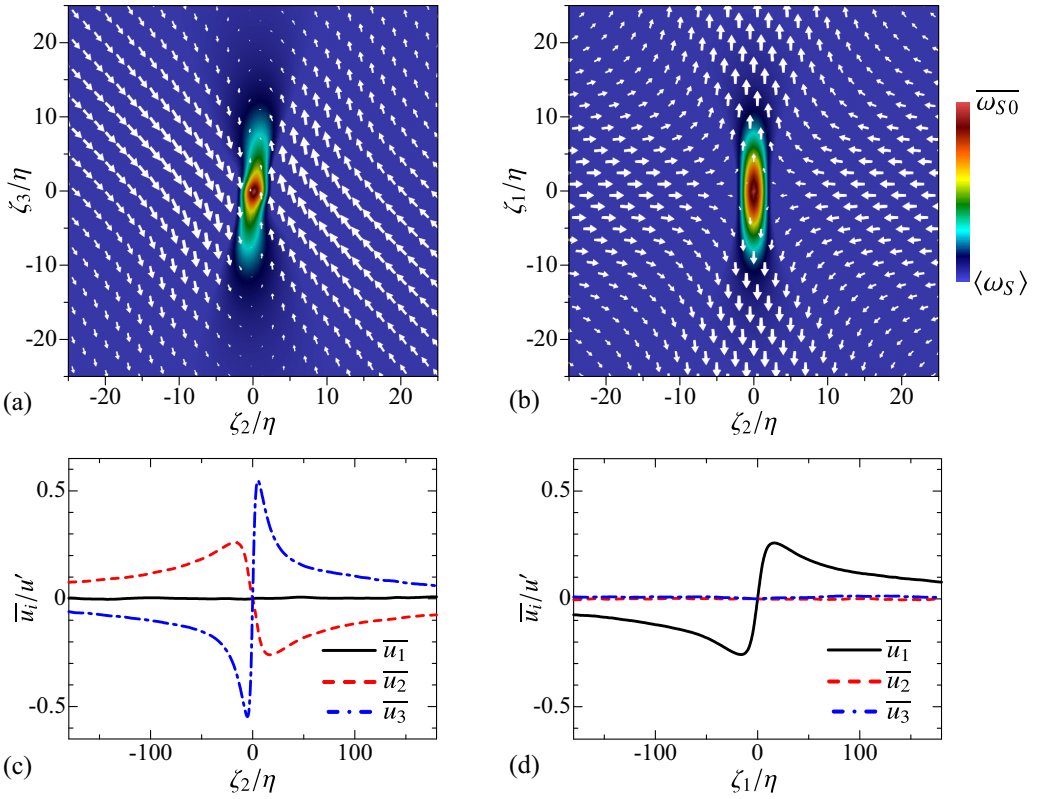

FIG. 2. Color contour of $\overline{\omega_S}$ and mean velocity vectors on the two-dimensional shear coordinates: (a) (ζ_2, ζ_3) at $\zeta_1 = 0$ and (b) (ζ_1, ζ_2) at $\zeta_3 = 0$. Length of the vectors corresponds to the vector magnitude in each figure. $\overline{u_1}$, $\overline{u_2}$, and $\overline{u_3}$ plotted as functions of (c) ζ_2 at $(\zeta_1, \zeta_3) = (0, 0)$ and (d) ζ_1 at $(\zeta_2, \zeta_3) = (0, 0)$. These results are taken from NS3.

A following procedure is repeated for $(\boldsymbol{n}_2)_x = -1, -0.999, -0.998, \ldots, 1$ in order to identify the shear coordinate. The increment 0.001 is small enough because the results of the present analysis do not change with such a small value. For each value of $(\boldsymbol{n}_2)_x$, other components of $\boldsymbol{n}_2$ can be determined by solving equations $\boldsymbol{n}_2 \cdot \boldsymbol{n}_2 = 1$ and $\boldsymbol{n}_1 \cdot \boldsymbol{n}_2 = 0$. For some values of $(\boldsymbol{n}_2)_x$, the solution of these equations does not exist, and such values of $(\boldsymbol{n}_2)_x$ are not used for finding the shear coordinate. Then, $\boldsymbol{n}_3$ is determined by a vector product of $\boldsymbol{n}_1$ and $\boldsymbol{n}_2$. The shear tensor $\nabla \boldsymbol{u}_S$ is evaluated in the new coordinate system defined with $(\boldsymbol{n}_1, \boldsymbol{n}_2, \boldsymbol{n}_3)$ by using the transformation matrix from the original coordinate $\boldsymbol{x}$ to the new coordinate. The shear coordinate is obtained with $(\boldsymbol{n}_2)_x$ that yields the maximum value of $(\nabla \boldsymbol{u}_S)_{3,2}$ after the coordinate transformation among all $(\boldsymbol{n}_2)_x$ examined above.

Once the shear coordinate $(\zeta_1, \zeta_2, \zeta_3)$ is determined at a local maximum point of ω_S, flow variables on $(\zeta_1, \zeta_2, \zeta_3)$ are obtained from the DNS grid by using a third-order Lagrange polynomial interpolation. The flow around the local maxima of ω_S is analyzed with the relative velocity with respect to the origin of the shear coordinate, whose components in $(\zeta_1, \zeta_2, \zeta_3)$ directions are represented as (u_1, u_2, u_3). The same procedure is repeated for all points of local maxima of ω_S. An averaged flow field associated with shearing motions is studied with ensemble averages in the shear coordinate, where the average $\overline{*}$ is taken as a function of $(\zeta_1, \zeta_2, \zeta_3)$.

Figures 2(a) and 2(b) show a mean flow pattern on the two-dimensional shear coordinate by visualizing $\overline{\omega_S}$ and a mean velocity vector, where the subscript 0 refers to a value at $(\zeta_1, \zeta_2, \zeta_3) =$

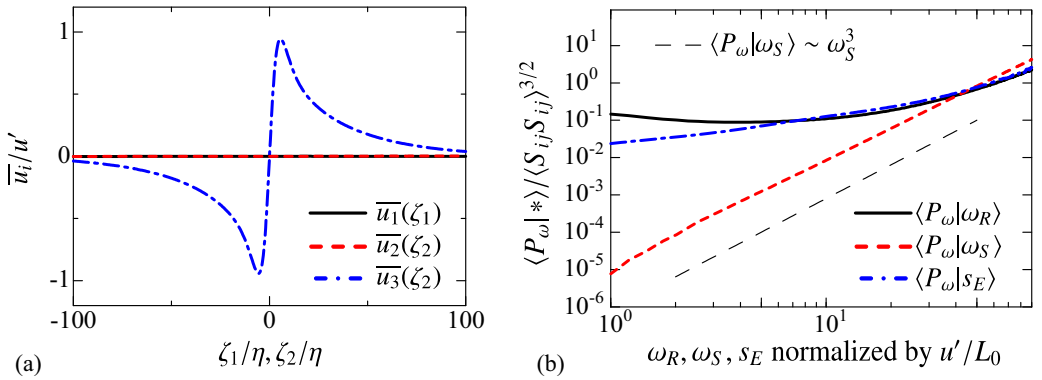

FIG. 3. (a) Mean velocity around local maxima of ω_S in random velocity R1, where $\overline{u_2}$ and $\overline{u_3}$ at $(\zeta_1, \zeta_3) = (0, 0)$ are plotted against ζ_2 while $\overline{u_1}$ at $(\zeta_2, \zeta_3) = (0, 0)$ is plotted against ζ_1. (b) Average of enstrophy production P_ω conditioned on ω_S, ω_R, or s_E in NS3, where an average of f conditioned on A is denoted by $\langle f|A\rangle$.

$(0, 0, 0)$. The averaged velocity vector exhibits a shear layer pattern, where two parallel flows in $\pm\zeta_3$ directions form the shear layer centered at $(\zeta_1, \zeta_2, \zeta_3) = (0, 0, 0)$. Figures 2(c) and 2(d) show the mean velocity components on ζ_2 at $(\zeta_1, \zeta_3) = (0, 0)$ and on ζ_1 at $(\zeta_2, \zeta_3) = (0, 0)$, respectively. $\overline{u_2}$ and $\overline{u_3}$ on ζ_2 and $\overline{u_1}$ on ζ_1 rapidly change within the shear layer. Once these velocity components reach their peak near the center of the shear layer, they decrease as being away from the shear layer because of influences of a flow region that is not related to the shearing motion of interest. The mean velocity in Fig. 2 approaches 0 slowly with the distance from the shear layer, implying influences of large-scale motions on the shear layer. It is noteworthy that negative $\partial\overline{u_2}/\partial\zeta_2$ and positive $\partial\overline{u_1}/\partial\zeta_1$ in the shear layer are associated with a fluid deformation without shear, confirming the existence of a biaxial strain field with compression in the ζ_2 direction and stretching in the ζ_1 direction as also visualized in Fig. 2(b). This picture of the thin shear layer sustained by compression of the biaxial strain is consistent with Burgers' vortex layer [1], whose shear vorticity is expressed by $\omega_S = \partial u_3/\partial\zeta_2 = \omega_0 \exp(-\zeta_2^2/\delta^2)$ while its velocity field is given by $u_1 = \alpha\zeta_1$, $u_2 = -\alpha\zeta_2$, and $u_3 = A\,\mathrm{erf}(\zeta_2/\delta)$. Here, α is the constant strain rate and $\delta = \sqrt{2\nu/\alpha}$ is the thickness of Burgers' vortex layer. This velocity profile is also qualitatively valid within the shear layer as attested by large values of $\partial\overline{u_2}/\partial\zeta_2 < 0$, $\partial\overline{u_3}/\partial\zeta_2 > 0$, and $\partial\overline{u_1}/\partial\zeta_1 > 0$. The mean flow pattern of the shear layer is qualitatively similar for all Reynolds numbers (not shown here). Hereafter, the difference between positive and negative peaks of $\overline{u_1}$ on ζ_1 in Fig. 2(d) is denoted by Δu_1, and the distance between these peaks is by δ_1. Similarly, Δu_2 and Δu_3 represent, respectively, the difference in the peaks of $\overline{u_2}$ and $\overline{u_3}$ on ζ_2 while δ_2 and δ_3 are the distances between the peaks.

Figure 3(a) shows the mean velocity around the local maxima of ω_S in random velocity R1, where $\overline{u_1}(\zeta_1, 0, 0)$, $\overline{u_2}(0, \zeta_2, 0)$, and $\overline{u_3}(0, \zeta_2, 0)$ are plotted against ζ_1 or ζ_2. In real turbulent flows (Fig. 2), these velocity components exhibit large peaks around $(\zeta_1, \zeta_2, \zeta_3) = (0, 0, 0)$. Although the random velocity has a velocity jump for $\overline{u_3}$ associated with the shear, the biaxial strain caused by $\overline{u_1}$ and $\overline{u_2}$ does not exist as attested by $\overline{u_1} \approx 0$ and $\overline{u_2} \approx 0$. Therefore, the shearing motions arise from a purely kinematic nature of the velocity field while the biaxial strain acting on the shear is due to the dynamical property of turbulence, which is the consequence of the Navier-Stokes equations. The extensive strain $\partial\overline{u_1}/\partial\zeta_1$ of the biaxial strain results in vortex stretching for vorticity of the shear, which contributes to enstrophy production $P_\omega = \omega_i S_{ij} \omega_j$ (ω_i, vorticity vector; S_{ij}, rate-of-strain tensor). Figure 3(b) shows averages of P_ω conditioned on the shear, rotation, and elongation intensities evaluated as ω_S, ω_R, and s_E, respectively. Here, the conditional average is calculated in the entire computational domain. The average of P_ω has a stronger dependence on ω_S than ω_R and s_E, and increases roughly with ω_S^3. The mean flow pattern of shearing motions as well as the conditional

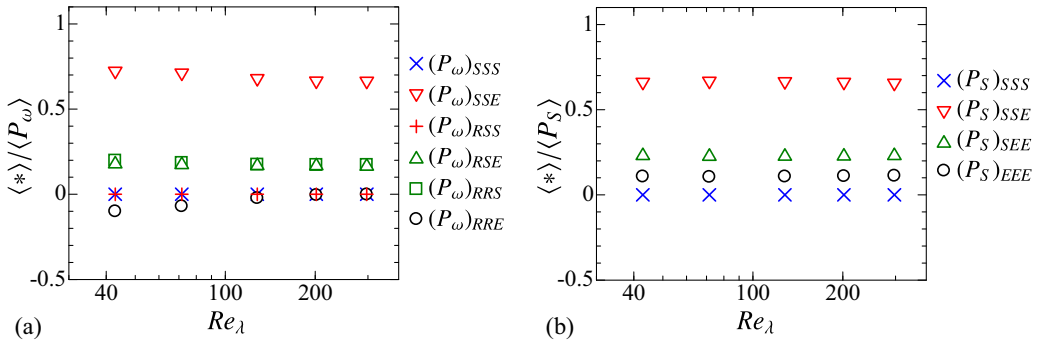

FIG. 4. Averages of decomposed terms of (a) $P_\omega = \omega_i S_{ij} \omega_j$ and (b) $P_S = -S_{ij} S_{jk} S_{ki}$.

average of P_ω indicate that the shearing motions have an important contribution to the enstrophy production. It is known that the random velocity field has zero mean enstrophy production [23], which is consistent with the absence of vortex stretching due to the interplay between the biaxial strain and shearing motions in Fig. 3(a).

Enstrophy production $P_\omega = \omega_i S_{ij} \omega_j$ and strain self-amplification $P_S = -S_{ij} S_{jk} S_{ki}$ have been extensively studied for understanding the small-scale dynamics of turbulence [24–26]. Their contribution to the energy cascade process is also investigated in recent studies [27]. These terms can be expressed by the tensor components obtained by the triple decomposition, where $P_\omega = \omega_i S_{ij} \omega_j$ is written as

$$P_\omega = (P_\omega)_{SSS} + (P_\omega)_{SSE} + (P_\omega)_{RSS} + (P_\omega)_{RSE} + (P_\omega)_{RRS} + (P_\omega)_{RRE}, \tag{2}$$

where

$$(P_\omega)_{SSS} = (\omega_S)_i (\omega_S)_j (S_S)_{ij}; \quad (P_\omega)_{SSE} = (\omega_S)_i (\omega_S)_j (\nabla \boldsymbol{u}_E)_{ij};$$
$$(P_\omega)_{RSS} = 2(\omega_R)_i (\omega_S)_j (S_S)_{ij}; \quad (P_\omega)_{RSE} = 2(\omega_R)_i (\omega_S)_j (\nabla \boldsymbol{u}_E)_{ij};$$
$$(P_\omega)_{RRS} = (\omega_R)_i (\omega_R)_j (S_S)_{ij}; \quad (P_\omega)_{RRE} = (\omega_R)_i (\omega_R)_j (\nabla \boldsymbol{u}_E)_{ij}.$$

Here, $(S_S)_{ij} = [(\nabla \boldsymbol{u}_S)_{ij} + (\nabla \boldsymbol{u}_S)_{ji}]/2$ is a symmetric part of the shear tensor. Similarly, $P_S = -S_{ij} S_{jk} S_{ki}$ is decomposed into four terms:

$$P_S = (P_S)_{SSS} + (P_S)_{SEE} + (P_S)_{SSE} + (P_S)_{EEE}, \tag{3}$$

where

$$(P_S)_{SSS} = -(S_S)_{ij} (S_S)_{jk} (S_S)_{ki}; \quad (P_S)_{SEE} = -3(S_S)_{ij} (\nabla \boldsymbol{u}_E)_{jk} (\nabla \boldsymbol{u}_E)_{ki};$$
$$(P_S)_{SSE} = -3(S_S)_{ij} (S_S)_{jk} (\nabla \boldsymbol{u}_E)_{ki}; \quad (P_S)_{EEE} = -(\nabla \boldsymbol{u}_E)_{ij} (\nabla \boldsymbol{u}_E)_{jk} (\nabla \boldsymbol{u}_E)_{ki}.$$

Averages of P_ω and P_S are known to be positive in turbulence [24]. Figure 4 shows the averages of each term divided by $\langle P_\omega \rangle$ or $\langle P_S \rangle$ against Re_λ. The relative contribution of these terms hardly depends on the Reynolds number. $(P_\omega)_{RRE}$ and $(P_S)_{EEE}$ do not contain the shear tensor, and their averages have a small contribution to $\langle P_\omega \rangle$ and $\langle P_S \rangle$, respectively. The terms arising solely from the shear tensor, $(P_\omega)_{SSS}$ and $(P_S)_{SSS}$, are 0, and the shearing motion itself does not cause the enstrophy production and strain self-amplification without interacting with other motions. On the other hand, the terms associated with the interaction between shear and elongation, $(P_\omega)_{SSE}$ and $(P_S)_{SSE}$, have a major contribution to averages of P_ω and P_S. For the shear layer pattern in Fig. 2, the interaction between the shear $(\partial \overline{u_3}/\partial \zeta_2 > 0)$ and the compressive component of the biaxial strain $(\partial \overline{u_2}/\partial \zeta_2 < 0)$ results in large positive $-(S_S)_{23} (S_S)_{32} (\nabla \boldsymbol{u}_E)_{22}$, which is one of the components of $(P_S)_{SSE}$. As already discussed above, the mean flow pattern in Fig. 2 causes vortex stretching due to the interplay between the biaxial strain and shearing motions, which results in large positive $(P_\omega)_{SSE}$.

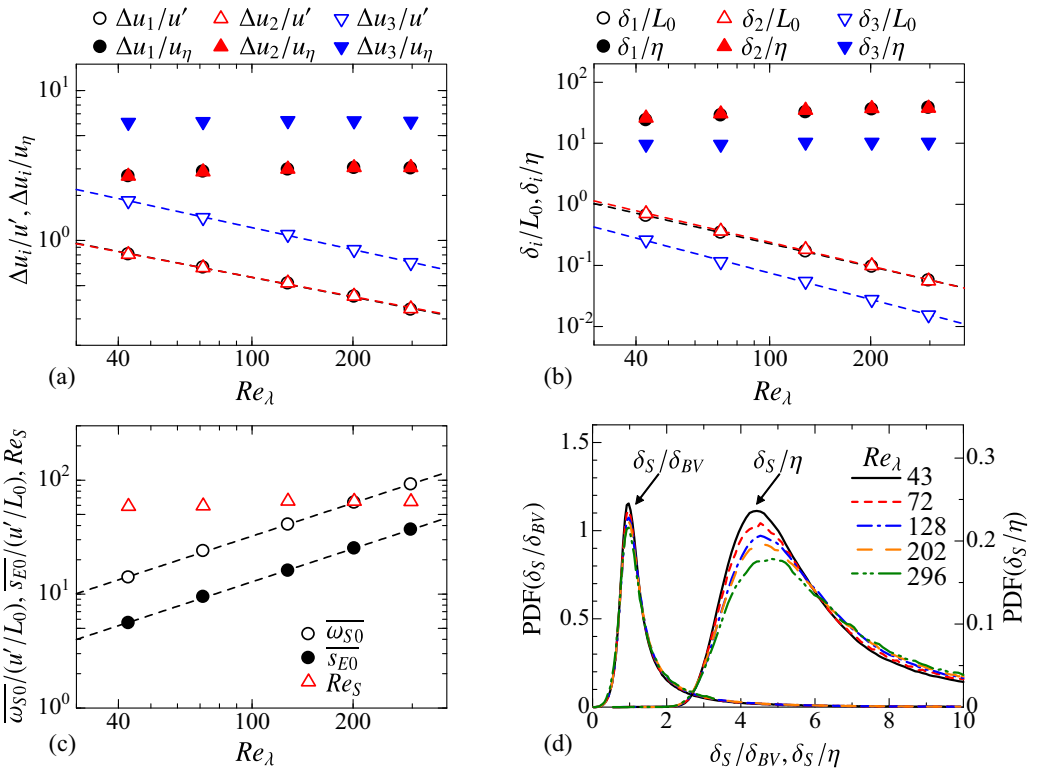

FIG. 5. Re_λ dependence of shear layers in NS1–5. (a) Velocity jumps Δu_1, Δu_2, and Δu_3 normalized by u_η or u'. (b) Length scales δ_1, δ_2, and δ_3, normalized by η or L_0. (c) Shear and strain intensities, $\overline{\omega_{S0}}$ and $\overline{s_{E0}}$, normalized by u'/L_0 and shear Reynolds number Re_S. Broken lines represent power laws obtained by a least-square method. (d) PDFs of shear layer thickness δ_S divided by the Kolmogorov scale η or the Burgers' vortex layer thickness δ_{BV}.

These results indicate the importance of the interaction between shearing motions and elongation (irrotational straining motion) in the amplification of vorticity and strain fields.

Figures 5(a)–5(c) show the Reynolds number dependence of the shear layer observed in the mean flow around shearing motions. Figures 5(a) and 5(b) plot Δu_i and δ_i against Re_λ, where $u_\eta = (\nu\varepsilon)^{1/4}$ is the Kolmogorov velocity. One can observe power-law behaviors of $\Delta u_i/u' \sim \mathrm{Re}_\lambda^{-a_i}$ and $\delta_i/L_0 \sim \mathrm{Re}_\lambda^{-b_i}$. A least-square method yields $a_1 = 0.44$, $a_2 = 0.43$, $a_3 = 0.49$, $b_1 = 1.3$, $b_2 = 1.3$, and $b_3 = 1.4$. Figure 5(c) shows mean intensities of the shear and biaxial strain $\overline{\omega_{S0}}$ and $\overline{s_{E0}}$. As expected from the power-law behaviors of δ_i and Δu_i, $\overline{\omega_{S0}}$ and $\overline{s_{E0}}$ also increase with $(u'/L_0)\mathrm{Re}_\lambda^c$, where the least-square method yields $c = 0.97$ for both $\overline{\omega_{S0}}$ and $\overline{s_{E0}}$. Kolmogorov scaling of these quantities requires $a = 0.5$, $b = 1.5$, and $c = 1$ [28], which are close to the exponents in the present DNS. Figure 5(c) also shows the Reynolds number of the shear layer $\mathrm{Re}_S = \Delta u_3 \delta_3/\nu$, which can be rewritten as $\mathrm{Re}_S = (\Delta u_3/u_\eta)(\delta_3/\eta)$. The averages of NS1–5 yield $\delta_3/\eta = 10.2$ and $\Delta u_3/u_\eta = 6.2$, and therefore $\mathrm{Re}_S \approx 63$. If the weak Re_λ dependence of $\Delta u_3/u_\eta$ and δ_3/η is taken into account, the present DNS yields $\mathrm{Re}_S \sim \mathrm{Re}_\lambda^{0.06}$, which hardly changes with Re_λ. Extrapolation of the present results suggests $\mathrm{Re}_S = O(10^1)$ for a wide range of Re_λ.

A shear layer structure was previously observed in a mean flow pattern taken in the local coordinate defined by the eigenvectors of the strain rate tensor (strain eigenframe) [29,30]. Unlike the present study, their average in the strain eigenframe is not conditioned on shearing motions. The Reynolds number dependence of the mean flow pattern in the strain eigenframe was examined in [31], where the velocity jump across the shear layer structure was about $5.5u_\eta$, which hardly depends

on the Reynolds number for $30 < \mathrm{Re}_\lambda < 1200$. This scaling of the velocity jump agrees with the present result $\Delta u_3 \approx 6.2 u_\eta$, which is obtained by identifying shearing motions from instantaneous flow fields. The shear layer pattern found in the strain eigenframe indicates that the strain eigenframe is strongly influenced by the shear orientation because the shear tensor contribution to S_{ij} is larger than the elongation tensor $\nabla \boldsymbol{u}_E$ in most parts of turbulent flows [17].

Beronov and Kida [32] presented a linear stability analysis of Burgers' vortex layer with perturbations. Their analysis suggests that the shear layer with $\mathrm{Re}_S \approx 63$ detected in this study is unstable for perturbations in turbulence, and a roll-up of the shear layers can occur to form vortex tubes. Furthermore, the perturbations in the shear layer can grow with a timescale of $\delta_3/\Delta u_3 = [(\delta_3/\eta)/(\Delta u_3/u_\eta)]\tau_\eta \sim T_0 \mathrm{Re}_\lambda^{-1}$, where $T_0 = L_0/u'$ is the large-scale eddy turnover time. Therefore, the perturbations of the shear layer in turbulence grows with the Kolmogorov timescale τ_η, which is much shorter than large-scale turbulent motions. Indeed, Figs. 1(b)–1(e) confirm that a region with strong shear evolves with time and forms a vortex tube within several times of τ_η.

The thickness of each shear layer can be estimated as the halfwidth of ω_S, which is obtained as a distance δ_S between two points of $\omega_S/\omega_{S0} = 0.5$ on the ζ_2 axis. Burgers' vortex layer has a halfwidth of ω_S given by $\delta_{\mathrm{BV}} = 1.67\sqrt{2\nu/\alpha}$. Here, α is associated with the elongation $\nabla \boldsymbol{u}_E$, and Burgers' vortex layer satisfies $\alpha = s_E/2$. For each point with local maxima of ω_S, the shear layer thickness δ_S and Burgers' vortex layer thickness $\delta_{\mathrm{BV}} = 1.67\sqrt{4\nu/s_E}$ are obtained with the profile of ω_S on the ζ_2 axis and s_E at the origin of the shear coordinate. Figure 1(d) shows the probability density functions (PDFs) of δ_S/η and $\delta_S/\delta_{\mathrm{BV}}$. A peak appears for $\delta_S/\eta \approx 4.5$ for all Re_λ. The PDF of $\delta_S/\delta_{\mathrm{BV}}$ has a peak at $\delta_S/\delta_{\mathrm{BV}} \approx 1$, indicating that the shear layer thickness is predicted well by Burgers' vortex layer. Thus, Burgers' vortex layer provides a good approximation for the relation between the elongation intensity s_E and the local shear layer thickness.

In summary, we have shown the statistical characteristics of shearing motions in isotropic turbulence. The triple decomposition is used for decomposing the velocity gradient tensor into three components representing an irrotational straining motion (elongation), a rotating motion, and a shearing motion. The mean flow pattern around the shearing motions confirms that the thin shear layer is sustained by the biaxial strain, in agreement with Burgers' vortex layer, which also predicts well the shear layer thickness. Shearing motions exist even in a random velocity field. However, the biaxial strain acting on the shear is caused by the dynamical property of the Navier-Stokes equations. The interplay between the shear and biaxial strain has an important contribution to enstrophy production and strain self-amplification. The velocity jumps associated with shearing motions exhibit the scaling $\Delta u_3/u' \sim \mathrm{Re}_\lambda^{-a_3}$ and $\delta_3/L_0' \sim \mathrm{Re}_\lambda^{-b_3}$, where the exponents are close to the values of Kolmogorov scaling. The shear Reynolds number $\mathrm{Re}_S \approx 60$ changes very slowly with Re_λ. $\mathrm{Re}_S \approx 60$ is large enough to the cause formation of vortex tubes from the shearing motions as visibly confirmed in this study, where the timescale of the vortex formation $\delta_3/\Delta u_3$ is of the order of the Kolmogorov timescale. The very weak dependence of Re_S on Re_λ indicates that small-scale vortex formations from shearing motions universally occur in turbulence for a wide range of Reynolds number.

ACKNOWLEDGMENTS

The authors would like to thank Prof. C. B. da Silva for discussion on the triple decomposition of three-dimensional velocity gradient tensors. This work was supported by JSPS KAKENHI Grants No. 18K13682, No. 18H01367, and No. 19J12973 and by "Collaborative Research Project on Computer Science with High-Performance Computing in Nagoya University." Some of the numerical simulations presented in this Rapid Communication were carried out on the high-performance computing system (NEC SX-ACE) at the Japan Agency for Marine-Earth Science and Technology.

[1] P. A. Davidson, *Turbulence: An Introduction for Scientists and Engineers* (Oxford University Press, New York, 2004).
[2] E. D. Siggia, Numerical study of small-scale intermittency in three-dimensional turbulence, J. Fluid Mech. **107**, 375 (1981).
[3] R. A. Antonia, E. J. Hopfinger, Y. Gagne, and F. Anselmet, Temperature structure functions in turbulent shear flows, Phys. Rev. A **30**, 2704 (1984).
[4] M. Kholmyansky, A. Tsinober, and S. Yorish, Velocity derivatives in the atmospheric surface layer at $\mathrm{Re}_\lambda = 10^4$, Phys. Fluids **13**, 311 (2001).
[5] J. Jiménez, A. A. Wray, P. G. Saffman, and R. S. Rogallo, The structure of intense vorticity in isotropic turbulence, J. Fluid Mech. **255**, 65 (1993).
[6] A. Tsinober, *An Informal Conceptual Introduction to Turbulence* (Springer, New York, 2009).
[7] J. M. Burgers, A mathematical model illustrating the theory of turbulence, Adv. Appl. Mech. **1**, 171 (1948).
[8] S. Kida and H. Miura, Identification and analysis of vortical structures, Eur. J. Mech. B **17**, 471 (1998).
[9] M. Tanahashi, S. Iwase, and T. Miyauchi, Appearance and alignment with strain rate of coherent fine scale eddies in turbulent mixing layer, J. Turbulence **2**, 1 (2001).
[10] C. B. da Silva, R. J. N. Dos Reis, and J. C. F. Pereira, The intense vorticity structures near the turbulent/non-turbulent interface in a jet, J. Fluid Mech. **685**, 165 (2011).
[11] A. Vincent and M. Meneguzzi, The dynamics of vorticity tubes in homogeneous turbulence, J. Fluid Mech. **258**, 245 (1994).
[12] T. Passot, H. Politano, P. L. Sulem, J. R. Angilella, and M. Meneguzzi, Instability of strained vortex layers and vortex tube formation in homogeneous turbulence, J. Fluid Mech. **282**, 313 (1995).
[13] B. Dubrulle, Beyond Kolmogorov cascades, J. Fluid Mech. **867**, P1 (2019).
[14] K. Horiuti, A classification method for vortex sheet and tube structures in turbulent flows, Phys. Fluids **13**, 3756 (2001).
[15] V. Kolář, Vortex identification: New requirements and limitations, Int. J. Heat Fluid Flow **28**, 638 (2007).
[16] J. Eisma, J. Westerweel, G. Ooms, and G. E. Elsinga, Interfaces and internal layers in a turbulent boundary layer, Phys. Fluids **27**, 055103 (2015).
[17] R. Nagata, T. Watanabe, K. Nagata, and C. B. da Silva, Triple decomposition of velocity gradient tensor in homogeneous isotropic turbulence, Comput. Fluids **198**, 104389 (2020).
[18] P. L. Carroll and G. Blanquart, A proposed modification to Lundgren's physical space velocity forcing method for isotropic turbulence, Phys. Fluids **25**, 105114 (2013).
[19] T. Watanabe and K. Nagata, Integral invariants and decay of temporally developing grid turbulence, Phys. Fluids **30**, 105111 (2018).
[20] A. Kempf, M. Klein, and J. Janicka, Efficient generation of initial- and inflow-conditions for transient turbulent flows in arbitrary geometries, Flow, Turbul. Combust. **74**, 67 (2005).
[21] T. Watanabe, J. J. Riley, K. Nagata, R. Onishi, and K. Matsuda, A localized turbulent mixing layer in a uniformly stratified environment, J. Fluid Mech. **849**, 245 (2018).
[22] C. P. Caulfield and W. R. Peltier, The anatomy of the mixing transition in homogeneous and stratified free shear layers, J. Fluid Mech. **413**, 1 (2000).
[23] A. Tsinober and B. Galanti, Exploratory numerical experiments on the differences between genuine and "passive" turbulence, Phys. Fluids **15**, 3514 (2003).
[24] B. Galanti and A. Tsinober, Self-amplification of the field of velocity derivatives in quasi-isotropic turbulence, Phys. Fluids **12**, 3097 (2000).
[25] B. Lüthi, A. Tsinober, and W. Kinzelbach, Lagrangian measurement of vorticity dynamics in turbulent flow, J. Fluid Mech. **528**, 87 (2005).
[26] C. Meneveau, Lagrangian dynamics and models of the velocity gradient tensor in turbulent flows, Annu. Rev. Fluid Mech. **43**, 219 (2011).
[27] M. Carbone and A. D. Bragg, Is vortex stretching the main cause of the turbulent energy cascade? J. Fluid Mech. **883**, R2 (2020).
[28] S. B. Pope, *Turbulent Flows* (Cambridge University Press, Cambridge, UK, 2000).

[29] G. E. Elsinga and I. Marusic, Universal aspects of small-scale motions in turbulence, J. Fluid Mech. **662**, 514 (2010).

[30] G. E. Elsinga and C. B. da Silva, How the turbulent/non-turbulent interface is different from internal turbulence, J. Fluid Mech. **866**, 216 (2019).

[31] G. E. Elsinga, T. Ishihara, M. V. Goudar, C. B. da Silva, and J. C. R. Hunt, The scaling of straining motions in homogeneous isotropic turbulence, J. Fluid Mech. **829**, 31 (2017).

[32] K. N. Beronov and S. Kida, Linear two-dimensional stability of a Burgers vortex layer, Phys. Fluids **8**, 1024 (1996).